Journal of Applied Fluid Mechanics, Vol. 17, No. 12, pp. 2579-2591, 2024.
Available online at www.jafmonline.net, ISSN 1735-3572, EISSN 1735-3645.
https://doi.org/10.47176/jafm.17.12.2732

Experimental and Numerical Unsteady Aeroelastic Effect Analysis of Wing Model Triggered with Piezoelectric Material

F. Y. Comez[1†], N. Sengil[2] and D. F. Kurtulus[1]

[1] *Aerospace Engineering Department, Middle East Technical University, Ankara, Turkey*
[2] *Astronautical Engineering Department, University of Turkish Aeronautical Association, Ankara, Turkey*

Corresponding Author Email: yudumc@metu.edu.tr

ABSTRACT

The current study analyzed the piezoelectrically driven mechanism responsible for generating force in both rectangular and hummingbird wings, which mimicked the flapping motion of the micro air vehicles, utilizing a combination of numerical simulation and experimental approaches. Digital image correlation technology was employed within the experimental setup to capture the dynamic deformation pattern of the flapping wing, yielding dynamic deformation data. This dataset was subsequently integrated into the computational fluid dynamics (CFD) simulation software to explain the aeroelastic effects. In this way, the dynamic deformation data played a crucial role in computing inertial forces regarding wing flexibility. In addition, temporal force variations generated by the flapping wing were measured using a load cell. The numerical results provided a full understanding of the flapping wing's unsteady aerodynamics, with an emphasis on vortex formations and pressure distribution. We thoroughly examined the force produced by the piezo-actuated flapping wing system. This analysis was then rigorously compared with the data obtained from the load cell measurements. Our primary emphasis was on the vertical forces along the z-axis. Moreover, a thorough comparison of the combined CFD and experimental data inertial results revealed an overall agreement in the total forces from the load cell.

Article History

Received March 13, 2024
Revised May 19, 2024
Accepted June 30, 2024
Available online October 2, 2024

Keywords:

Experimental methods
Numerical methods
Flapping wing motion
Bioinspired MAVs
Digital image correlation

1. INTRODUCTION

Bioinspired flapping wing studies have met the requirements of potential micro air vehicle (MAV) designs for the last two decades. Numerous investigations have been conducted into the aerodynamic characteristics of flapping wings. Bioinspired studies can be divided into several categories, with primary features to consider when distinguishing. The lightweight, small size and propulsion efficiency are important points worth considering in terms of their effects. Birds generally employ wing flapping to create lift and thrust; however, the mechanism becomes more intricate in smaller flyers. They exhibit varied and complex flapping patterns, altering the angle of attack between the upstroke and downstroke phases. During hovering, hummingbirds exhibit a sinusoidal flapping motion with high-frequency values ranging from 100 Hz to 200 Hz. When these birds hover through flapping motions, they exhibit unsteady aerodynamic features. This allows them to remain in the air by generating enough force. The main emphasis of studying bio-inspired flapping wings' mechanical analysis and aerodynamics is comprehending the natural flyer's flight characteristics and ability to bear the load.

Due to their lightweight nature, piezoelectric actuators weighing only a few grams are considered one of the best sources of actuation in flapping-wing micro-air vehicles (FWMAVs). Instead of generating rotary motions with motor-driven systems, piezoelectric actuators produce vibratory motions and transform this vibration into artificial flapping wings with simple structures such as cantilevers or directly driven wings. These systems have provided a simple structure to drive the insect-scale FWMAVs (Quinn, 2022).

One of the piezoelectric actuators-driven dual-wing honeybee-sized insect scales with flapping motion is studied by James et al. (2018). The flapper is only 190 mg as a whole system. The maximum flapping amplitude is reached at a 170 Hz frequency value to create the maximum lift. A laser source is placed on top of the system to take off the flapping vehicle. A microcontroller is activated by obtaining power from the laser trigger, generating sinusoidal voltage outputs. Thus, electrical

inputs can supply two piezoelectric actuators to convert electric to mechanical motion.

On the other hand, Ozaki & Hamaguchi (2018) studied the tethered flight of directly driven wings using unimorph piezoelectric actuators. An external power source powers the two-wings prototype and takes off with a restriction based on 1 DOF. The total wingspan is 114 mm, and the total mass of the prototype is 598 mg. The lift force is measured at 100 V operating voltage of 665 mgf. During experimental measurements, an electric balance is used for average lift force data, and a camera simultaneously records the motion of the tethered system. The maximum stroke and pitch angles are 25.9° and 66.2°, respectively.

The other study of the bio-inspired flapping wing robot is Eristalis tenax (Zou et al., 2017). The bioinspired robot has four-bar systems with flexible hinges designed to serve as the transmission of the motion. The first take-off has one degree of freedom constraint by supporting a pair of vertical guide rails. The displacement of the wing tip is measured using a laser displacement sensor during experiments; at the same time, the resonant frequency of the piezoelectric actuator is identified. In this study, the wing consists of veins built from 60 μm thick carbon fiber due to its intrinsic high modulus and lightweight. Thus, the system weighs 84 mg, and the wingspan is 35 mm. The resonant frequency to take off is 100 Hz, and the driving signal is set to 250 V, generating sufficient thrust with an approximate ±60° flapping angle with ±380 μm vibration amplitude.

There are several active components to comprehend the nature of the wings, namely, the anisotropy due to the membrane and veins, and hinges endurance materials which result in the spanwise and the chordwise wing flexibility, and also the dorsal and the ventral flexibilities of the wing. As the flapping motion mechanism creates sufficient unsteady aerodynamic forces, flexible wings with airflow around them generate structural deformations on wings. Wing shape and wing deformation are crucial in lift generation during wing motion (Yang et al., 2022). Some distinct studies investigate the different aspects of flapping wing motions. An aeroelastic analysis can shed light on the bio-inspired fliers' secrets. To identify dynamic deformations of the flapping wing motion, unintrusive measurement systems have to be used to separate the characteristics of the flapping motion. One of the robust systems, digital image correlation (DIC), can be proposed to identify and measure the kinematic properties of the flapping motion of the bioinspired wings. This unintrusive system can be coupled with other measurement systems. Thus, several properties can be measured at one time.

In addition to the 3-D analysis, the aerodynamics of insect flying research in two dimensions efficiently highlight flow properties (Kurtulus et al., 2005; Kurtulus, 2022). Nonetheless, tip vortices, spanwise flow, and wing flexibility all substantially influence aerodynamic forces. Therefore, it is necessary to explore three-dimensional studies (Comez et al., 2024; Bektas et al., 2020; Senol et al., 2017). It is possible to conduct dynamic motion of the three-dimensional wing model using the experimental morphological and kinematic data from the flapping wing. Thus, these dynamic deformation data, such as spanwise twisting, in and out-of-plane bending, and their permutations, may be inspected and implemented into numerical studies as predefined motions. These numerical simulations mainly calculate the aerodynamic force generation part of the flapping wing motion in different flow conditions and obtain the flow structures using numerical methods (Dong et al., 2022; Yang et al., 2022). Furthermore, using predetermined motion via experimental techniques provides an appealing trade-off between computing costs and accuracy, making it particularly suitable for comparing computational structural dynamics in performing aeroelastic assessments. Dong et al. (2022) effectively proved the tool's validity by comparing particular results to those produced from existing numerical models based on Euler equations, vortex-lattice codes, and experimental data. In the study, utilizing the developed numerical framework and analyzing deformation mechanisms, two distinct effects emerged: wingspan twisting and in-plane bending influencing lift in localized zones of the stroke cycle. Furthermore, small-scale wing flights are particularly affected by the flexibility of the wing material, which influences the lift. Utilizing the unsteady vortex-lattice method in a comprehensive kinematic model shows an exact and efficient tool for forthcoming investigations into aeroelastic phenomena.

This paper begins by conducting experimental measurements to capture dynamic deformations of the wing and assess force characteristics during flapping motion. This is accomplished by employing the digital image correlation (DIC) method and measurements obtained from load cells. Subsequently, a dynamic motion of the flapping wing is constructed using experimental kinematic data. The dynamic motion data is subsequently incorporated into computational fluid dynamics (CFD) simulation software to investigate the aerodynamic force and the flow patterns surrounding the wing, considering the actual deformation patterns. Following this, the inertial forces of the flapping wing within the actual deformation pattern are determined utilizing dynamic deformation data. Finally, the outcomes are assessed and deliberated, encompassing aerodynamic forces, flow structures, inertial forces, and total forces.

2. EXPERIMENTAL METHODOLOGY

The goal of the experiments is to measure the deformations and forces of flexible aluminum material wings such as a rectangular and a Rufous hummingbird. To capture the deformations of the wings, a digital image correlation (DIC) camera system is used, and the vertical displacements (z-axis) are recorded (Fig. 1). During the experiments, the ATI Nano 17 load cell measures all six aerodynamic components (forces and torques along the x, y, and z axes) of force and torque. The maximum permissible overload values of the load cell range from 3.1 to 6.9 times the rated capacities. In addition, silicon strain gauges inside the load cell offer a signal strength 75 times greater than conventional foil gauges. By these features, the quality of the load cell is satisfactory for our experiments.

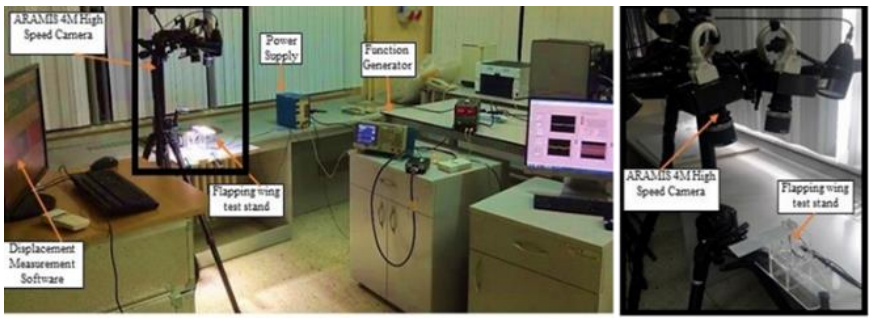

a) General view of experimental setup b) DIC system

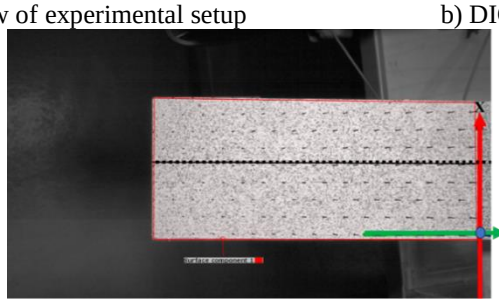

c) Close view of the rectangular wing seen by the DIC system

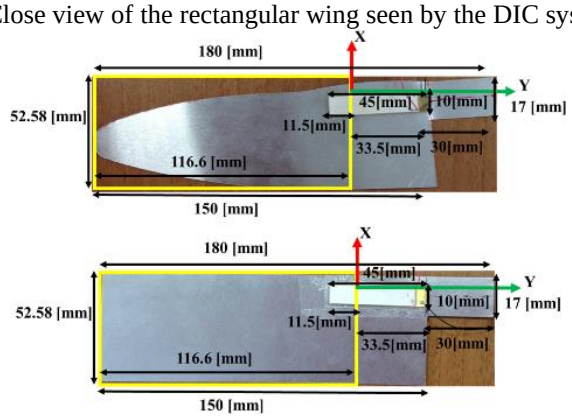

d) Close view of the rectangular wing and the Rufous hummingbird wing seen by the DIC system and their dimensions

Fig. 1 Experimental setup

Additionally, a bimorph bender piezoelectric actuator is utilized to trigger both wings. The dimensions and positions of the wings are presented in Fig. 1d, respectively. Using a piezoelectric trigger to generate displacement, we flapped our wings at frequencies ranging from 0 Hz to 20 Hz. Simultaneously, the force and dynamic deformation of the wings are measured using a dynamic deformation system.

The digital image correlation system's calibration relies on the wings' surface area and deformation. It is carried out with consideration of the sensor configuration formats section in the ARAMIS 4M hardware user guide (ARAMIS v6.3, 2009). The hardware settings were adjusted according to the 20 mm lens utilized in the experiment, as detailed in Table 1.

Table 1 ARAMIS 4M 20 mm lens properties (ARAMIS v6.3, 2011).

Sensor	ARAMIS 4M rev03
Lens	Titanar 20 mm
Measuring volume [mm^2]	250 × 180
Min. camera support length [mm]	500
Measuring distance [mm]	440
Slider distance [mm]	166
Camera angle [°]	25
Calibration object	CP20 250×200
Aperture-dependent depth of field [mm]	8 (aperture) >250

3. NUMERICAL METHODOLOGY

3.1 Morphological and Aerodynamic Parameters of Rectangular wing and Rufous hummingbird wing

The CFD simulation starts by reconstructing the models of the rectangular and Rufous hummingbirds in the computational flow domain. Solid models, the rectangular wing and Rufous hummingbird wing are scaled to a 7500 mm² (A) surface area. To mimic the real wing, the thickness is 0.4 mm (0.8% of the mean chord) (Wu & Ifju, 2010). For the Rufous hummingbird model, the key parameters are measured, such as the semi-span for a single wing from root to tip, 150 mm (R), and the mean chord and the non-dimensional parameter aspect ratio are calculated as 50 mm (c_m = A/(2R)) and 3, respectively (Table 2).

In the classification of literature, insects and small birds are considered capable of flying at significantly low

Table 2 Dimensional parameters of the wings in the current study

Parameter	Hummingbird and Rectangular wings
Forewing length (semi-span), R (mm)	150
Total wing area (single wing), A (mm^2)	7500
Mean aerodynamic chord, c_m =A/(R)	50
Aspect ratio, AR (R^2/A)	3

Table 3 Unsteady flow parameters of wings.

Parameter	Rectangular wing	Rufous hummingbird wing
Maximum wing tip velocity, U_{tip} (m/s)	0.6789	0.648
Air density, ρ (kg/m^3)	1.225	1.225
Dynamic viscosity, μ (kg/m. s)	1.7894×10^{-5}	1.7894×10^{-5}
Re = U_{tip}. ρ. c_m/ μ	2324	2218
Flapping frequency (Hz)	9.6	12.1
T=1/flapping frequency (s)	0.104	0.082

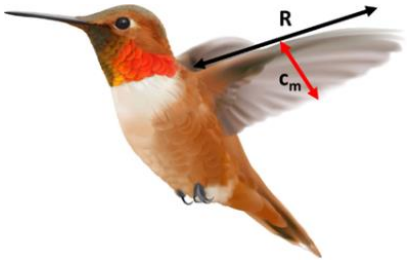

Fig. 2 Rufous hummingbird, in hover position. R is semi-wingspan length; c_m is the mean aerodynamic chord

Reynolds numbers. The flow conditions around these fliers are characterized as laminar flow (Shyy et al., 2013; Kurtulus, 2022; Dwivedi et al., 2022; Yang et al., 2022); therefore, numerical computations are performed using equations applicable to inviscid laminar flow cases for analysis in these scenarios (Table 3).

The user-defined function (UDF) is loaded and compiled to generate flapping motion in Ansys Fluent software (FLUENT 6.3, 2006). A simple periodic velocity profile equation is interpolated from the kinematic properties data obtained by DIC, and the flapping wing motion (ω) is given by Equation (1):

$$\omega = 2\pi\, \theta_{max} f_{flapping} \times \cos\left(2\pi f_{flapping} t\right) \times \sqrt{{}^{x}/_{l_{max}}} \quad (1)$$

As shown in Fig. 3, where θ_{max}, the maximum flapping angle in radians, $f_{flapping}$, the flapping frequency in Hz, ${}^{x}/_{l_{max}}$, and the x-nodes coordinate on the wing surface is divided by the length of the wing along the spanwise direction.

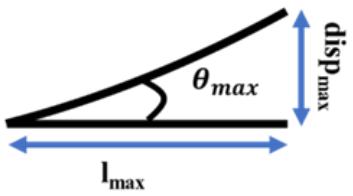

Fig. 3 Schematic displacement motion

3.2 Grid Sensitivity Study of the Rectangular Wing and Rufous Hummingbird Wing

In the current study, the wing morphological deformation data can be obtained in the experiments using DIC systems (Lau et al., 2020). Then, this deformation data is utilized as input to incorporate the aeroelastic influence into the CFD simulation. Moreover, in the study, a fluid spherical domain is constructed around the 3D wing model for numerical analysis of the flapping motion. Two O-type domains have been created, and the wing models are positioned within these domains, as depicted in Fig. 4a. In these domains, tetrahedral elements conform to the O-type mesh domain. A fine overset mesh is generated around the wing to improve computational accuracy during dynamic mesh motion, creating an inner domain in the shape of a sphere with a radius of 350 mm. Additionally, an outer spherical domain with a radius of 750 mm is constructed using coarser mesh elements. The far-field domain (outer sphere) has a pressure outlet boundary condition assigned as the boundary condition, and the wing surfaces are assigned the wall boundary condition.

Table 4 shows the total number of mesh elements for coarse (Mesh 1), medium (Mesh 2) and fine (Mesh 3) meshes. The wing models are investigated through instantaneous flapping motion displacements.

For the grid refinement analysis, maximum face sizing (inner region) is allocated to the wing surface with a specified growth rate of 1.2. The table shows that the face grid increases proportionately to the growth rate and extends to the inner domain's border. As a result, the outer domain's volume fills the gap between the two domains. Due to the dynamic flapping motion of the wing and computational limitations, three grid sizes are generated, and computations are performed using these varied grid configurations. Subsequently, the fine mesh cases are selected for all the simulations performed for both wing prototypes. Instantaneous aerodynamic variables are

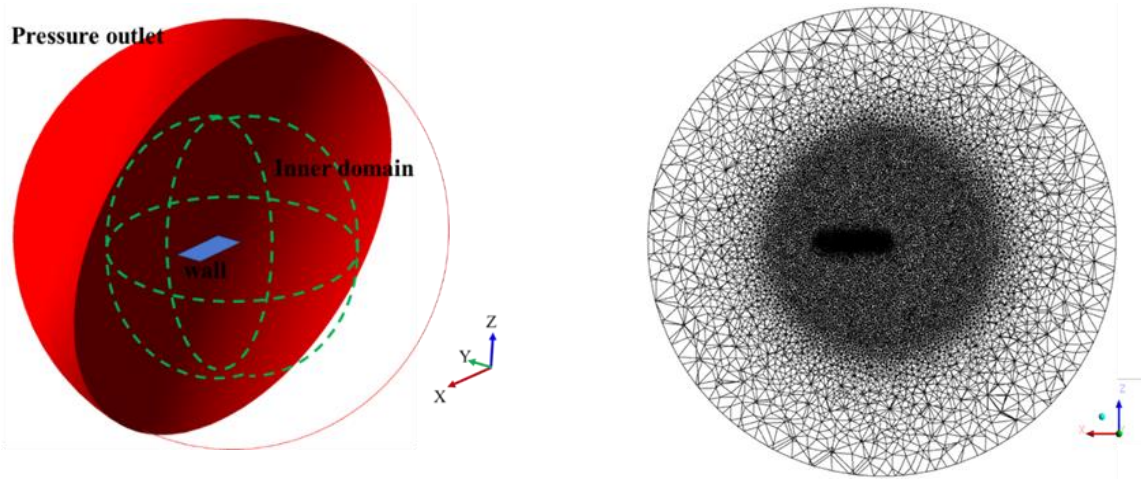

(a) (b)

Fig. 4 a) Flapping wing computational domain and boundary conditions, b) wing mesh domain

Table 4 The number of mesh elements of the wing models

Wing	Mesh type	Number of elements	Time step	Maximum Face Size [mm]
Rectangle	**Mesh 1**	1.022.700	Δt=0.0005 s	1.2
	Mesh 2	3.591.301		0.9
	Mesh 3	5.398.766		0.5
Rufous Hummingbird	**Mesh 1**	1.120.760	Δt=0.0004 s	1.2
	Mesh 2	3.820.346		0.9
	Mesh 3	5.198.700		0.6

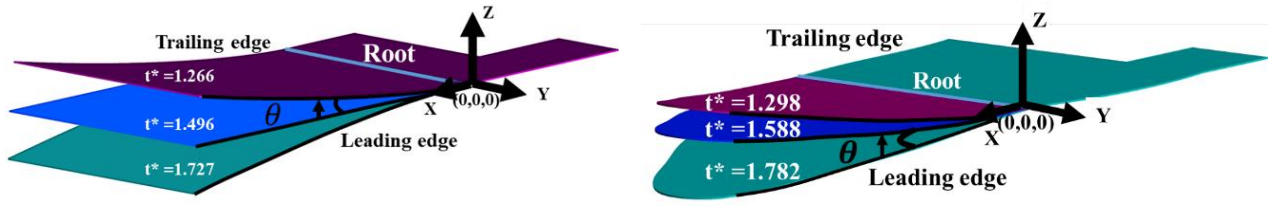

(a) (b)

Fig. 5 Maximum and minimum flapping wing positions a) Rectangular wing, b) Rufous wing

observed based on the simulations performed on fine meshes (Table 4).

The flapping angle is measured by the DIC system and found to vary between θ ϵ [-6º,6º] for the rectangular wing and θ ϵ [-5º,5º] for the hummingbird wing (Fig. 5).

The flapping frequency of the rectangular wing is 9.6 Hz, while that of the hummingbird is 12.1 Hz. We obtain 600 images with a shutter time of 120 Hz using the DIC system. Consequently, one flapping cycle is interpolated to 208 equidistant time intervals for the rectangular wing and 205 intervals for the hummingbird wing through sampling. The variation in the number of time intervals arises from the difference in their flapping frequencies, leading to distinct time points.

4. RESULTS

3.1 Forces

Fig. 6 and Fig. 7 illustrate the instantaneous vertical forces (z-axis) extracted from computational fluid dynamics (CFD) simulations concerning rectangular and hummingbird wing configurations, respectively. The figure of the rectangular wing configuration reveals that the instantaneous aerodynamic force in the z-direction is quantified at 0.0559 grams. In parallel, the Rufous hummingbird wing configuration demonstrates a slightly lower mean aerodynamic force, recorded at 0.0433 grams. This differential in force magnitudes underscores the distinct aerodynamic efficiencies inherent to each wing type.

A dynamic problem entails determining the force applied to the wing model based on its motion. When solving the problem, the second-order curve fits of the acceleration are integrated from the root to the tip of the wing. Newton's second law is applied to the Equation to calculate the inertial force acting on the wing. In the present scenario, the wing models' dynamic deformation (vertical displacement) and acceleration are directly measured during the experimental flapping process. To calculate the integral of the acceleration curve along the span of the wing, the trapezoidal function is called in MATLAB software.

$$\int_a^b acc(x)dx \approx \frac{1}{2}\sum_{n=1}^{N}(x_{n+1}-x_n)[acc_n(x)+acc_{n+1}(x)] \quad (2)$$

$$\vec{a}_{avg} = \int_a^b acc(x)dx\,/(length\ of\ wing) \quad (3)$$

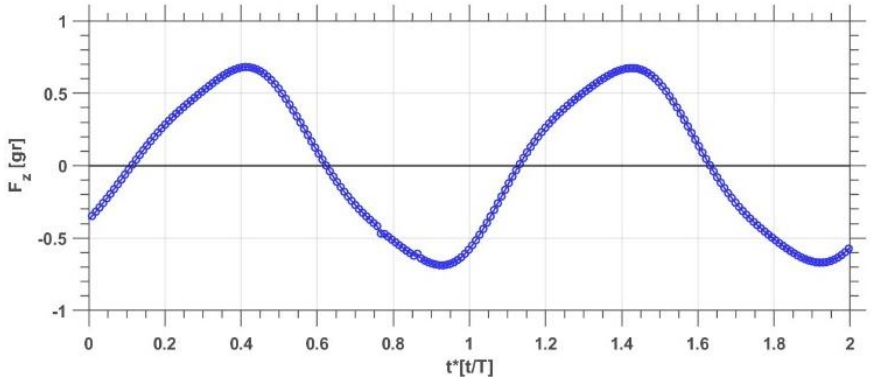

Fig. 6 Vertical force of the rectangle wing in z-direction direction

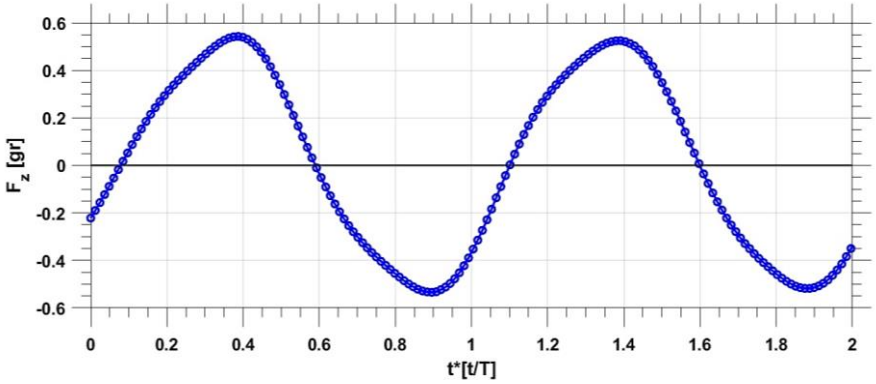

Fig. 7 Vertical force of Rufous hummingbird wing in z-direction

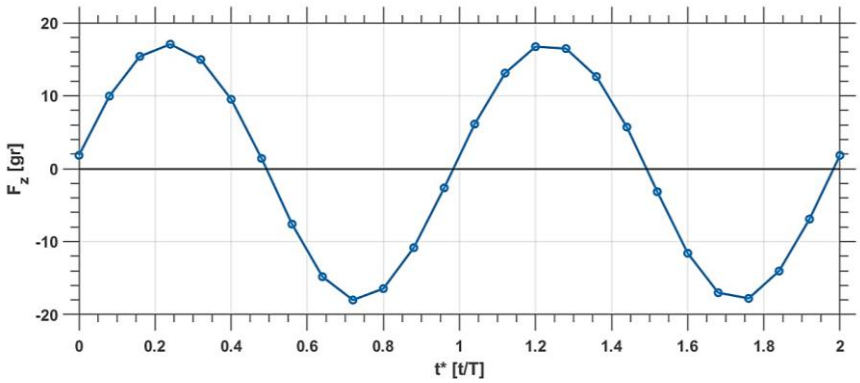

Fig. 8 Inertial force calculation by rectangular wing acceleration (DIC)

$$\vec{F} = m\,\vec{a}_{avg} \tag{4}$$

where the $a = x_1 < \cdots < x_N < x_{N+1} = b,$ and $(x_{n+1} - x_n)$ is the spacing between each consecutive pair of spanwise points. Subsequently, each wing position's average acceleration value is examined at every time step. The instantaneous accelerations of the wings are used to obtain the instantaneous inertial forces. In Fig. 8 and Fig. 9, these instantaneous inertial forces are displayed for two time periods. The time t is explored as a non-dimensional time denoted as t*=t/T, where T is the period of flapping motion given in Table 3.

It is important to note that the time instances t* = 0.25 and t* = 1.25 for the rectangular wing represent the maximum upstroke positions. These cases precisely correspond to the end of the upward motion and the beginning of the downward motion, as seen in Fig. 8. For the hummingbird, the upstroke of the wing begins at t*=0 and reaches its peak (t*=0.3) with maximal vertical positive force. The downstroke follows, gradually diminishing the force until it reaches its minimal value at t*= 0.8. This pattern continues till the end of the downstroke. This cyclic process occurs on succeeding up and down strokes, as demonstrated in Fig. 9.

Fig. 10 and Fig. 11 show the load cell vertical force measurements. These forces encompass both inertial and aerodynamic forces. The sum of inertial and aerodynamic forces represents the combined forces. These combined forces are compared with the total force data obtained from the load cell.

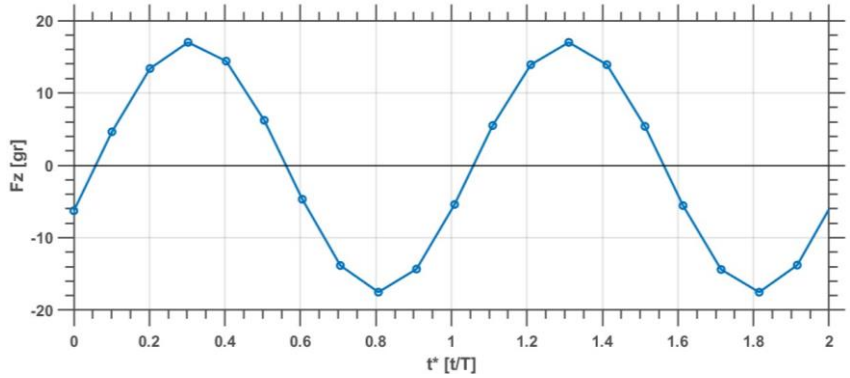

Fig. 9 Inertial force calculation by Rufous hummingbird wing acceleration (DIC)

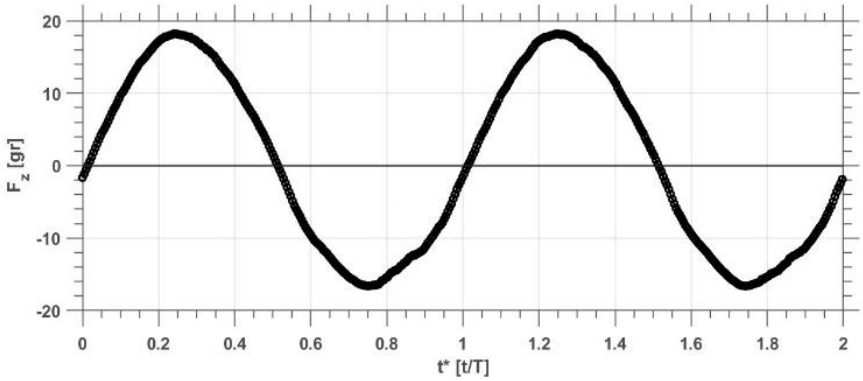

Fig. 10 Total force measurement in vertical direction [z-direction] of rectangle wing by the load cell

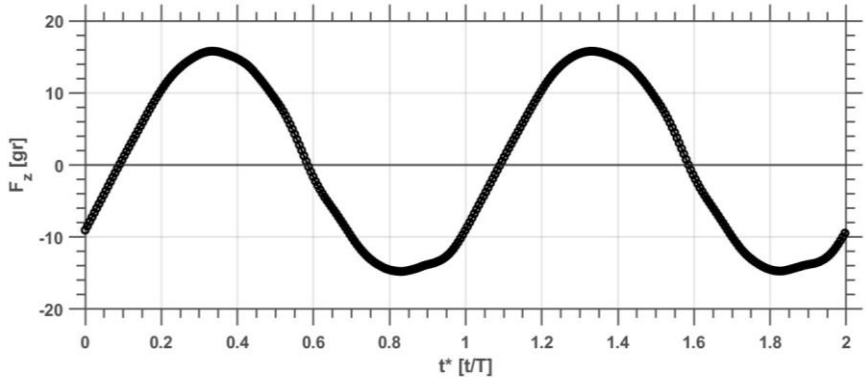

Fig. 11 Total force measurement in vertical direction [z-direction] of Rufous hummingbird wing by load cell

In Fig. 12 and Fig. 13, the experimental and numerical forces are found to be almost the same at the end of the upstroke and the beginning of the downstroke. However, a marginal discrepancy is observed between the sensor measurement and the total (CFD + Inertial) forces during the reverse motion, corresponding to the end of the downstroke and the beginning of the upstroke. This discrepancy is quantified as 11.6% in the case of the rectangular wing curves (Fig. 12), while the difference for the hummingbird wing is determined to be 14.8% (Fig. 13). The difference might be related to the incremental chordwise deformations of the wing tips during stroke reversals, which are not considered in CFD simulations.

3.2 Pressure Distribution

The second phase of the flapping movements is depicted in the rectangular and hummingbird wings in Fig. 14 and Fig. 16. In addition, concerning these motions, Fig. 15 and Fig. 17 depict the instantaneous pressure contours at specific time instances. High-pressure values occur on the wing's lower surface during the upstroke, reaching their peak when the wings are at their highest positions. The primary reason for the positive pressure underneath the wing is the movement of dominant tip vortices towards its lower surface during wing motion. After the upstroke, new vortices form on the lower surface while existing ones depart. This creates significant pressure differences on both surfaces. As a result, there is suction on the upper surface and dominant pressure on the lower surface. This is confirmed by the vertical force graphs (Fig. 12, Fig. 13), which show a positive vertical force on the wing.

When looking at the beginning of the downward movement, tip vortices still accumulate towards the wing tip, causing high-pressure values at the tip of the lower surface (Fig. 15, Fig. 17). As the wing approaches the middle of the downward motion, the pressure distribution on both surfaces becomes closer, resulting in negligible

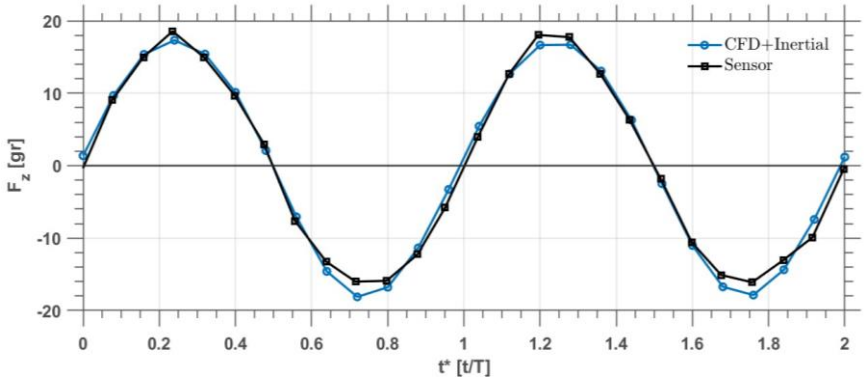

Fig. 12 Vertical force comparison between CFD and Inertial forces with sensor data in the z-direction (rectangle wing)

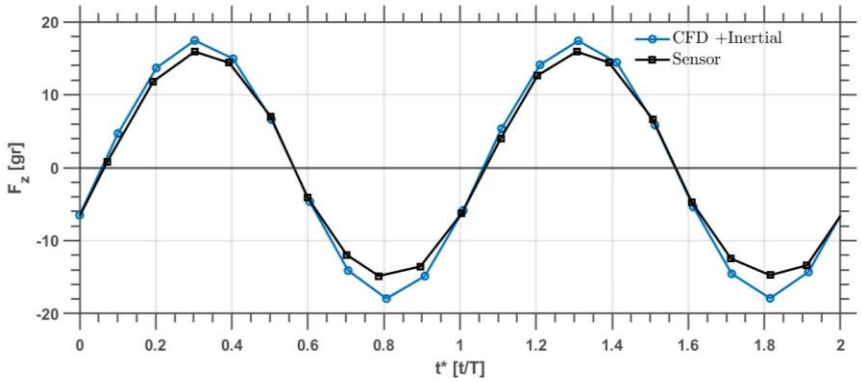

Fig. 13 Vertical force comparison between CFD and Inertial forces with sensor data in z-direction (Rufous hummingbird wing)

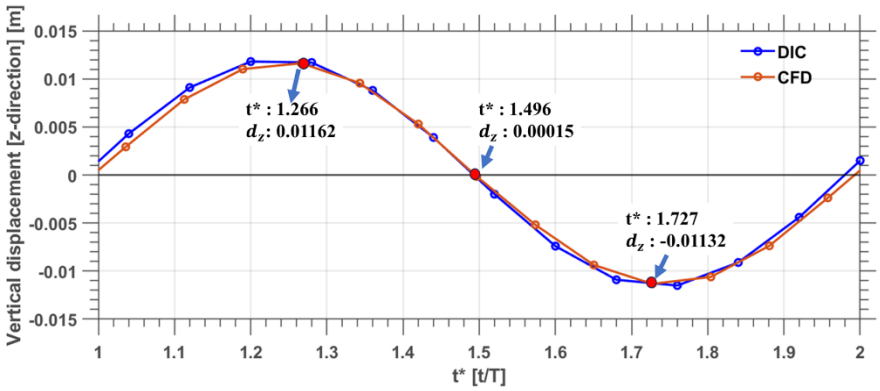

Fig. 14 One period of flapping motion of rectangle wing (2nd period of flapping motion)

force generation on average. Due to the persistent descent, vortices significantly impact the upper surface, creating a suction effect below, which leads to negative vertical force values on the wing, as illustrated in Fig. 12 and Fig. 13.

The leading-edge vortices (LEV) on the wing contribute to the pressure distributions on the upper and lower surfaces of the wing. As the wing begins its upward motion, counter-clockwise (CCW: red) vortices at the trailing edge grow and deflect downwards beneath the wing, while clockwise (CW: blue) vortices at the leading edge grow and turn towards the lower part of the wing (Fig. 17, Fig. 18). As the wing continues to move upward (Fig. 14), these vortices at the leading edge (LE) and trailing edge (TE) grow. These growing vortices also join the tip vortices, eventually separating from the wingtip.

Upon completion of the upward motion of the wing and initiation of the downward motion, new CCW vortices start forming as LEVs at the wing's leading edge. Simultaneously, CW vortices form at the trailing edge. As the wing moves downward, CW and CCW vortices grow on its upper surface in the opposite direction of the motion. When these CW and CCW vortices begin to detach from the wing, they form high-pressure contours on its upper surface. Subsequently, they accumulate and detach from the wingtip by joining the tip vortices from the wing's upper surface.

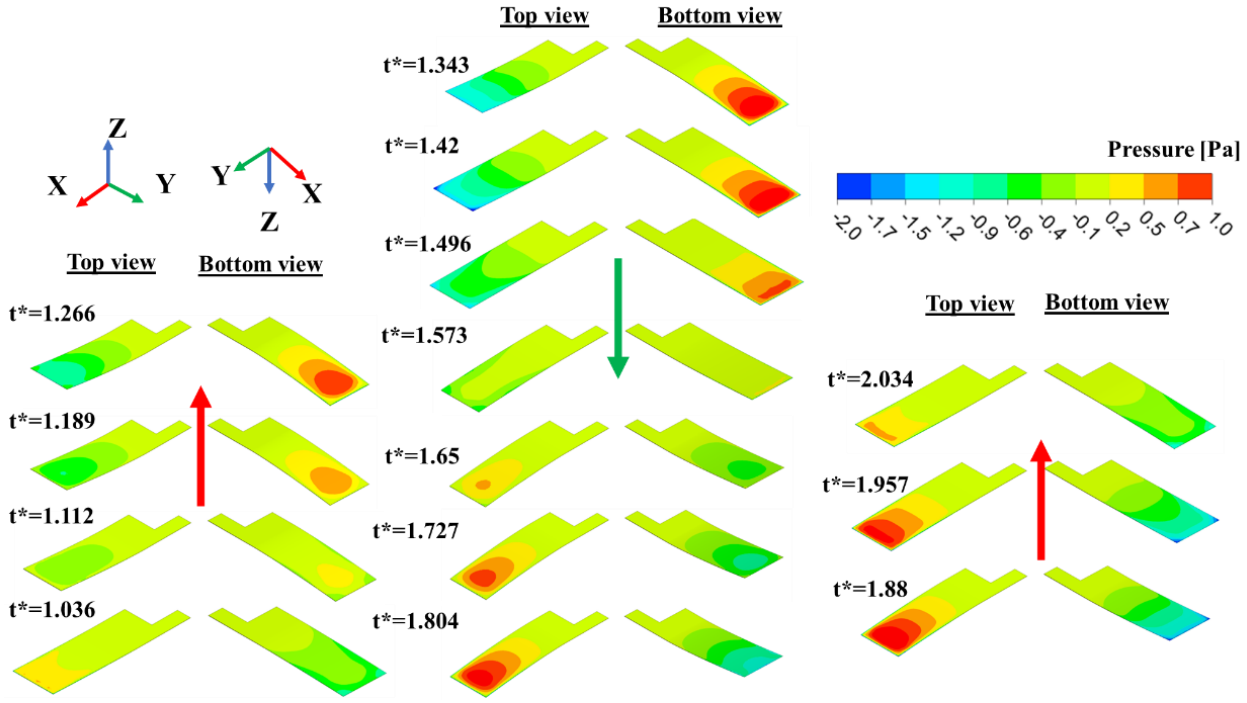

Fig. 15 Instantaneous pressure contours of rectangle wing (2nd period of flapping motion)

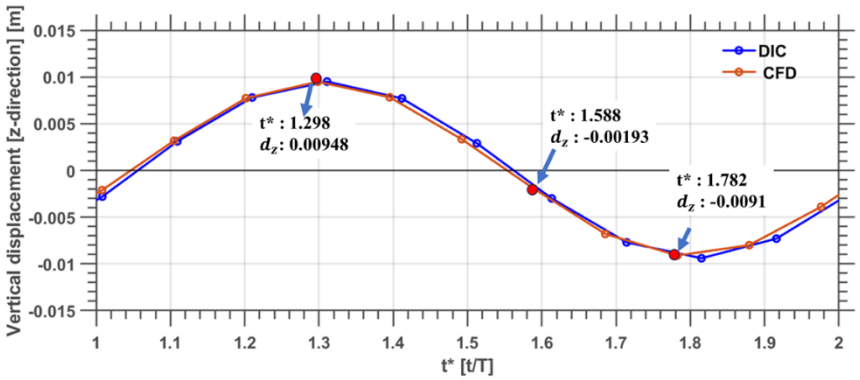

Fig. 16 One period of Rufous hummingbird wing flapping motion (2nd period of flapping motion)

In the case of the rectangular wing, at t*=1.266, a low-pressure area manifests on the upper wing surface due to the presence of the leading-edge vortex (LEV). In contrast, concurrently, a relatively significant high-pressure region develops on the lower surface (Fig. 15). Likewise, at t*=1.727, the high-pressure region migrates to the upper surface, accompanied by a low-pressure area on the lower surface (Fig. 15).

Additionally, in the case of the hummingbird wing (Fig. 16), at t*=1.298, a low-pressure region reappears on the upper surface due to the presence of the leading-edge vortex. In contrast, a comparatively significant high-pressure region emerges on the lower surface (Fig. 17). Likewise, at t*= 1.782, the high-pressure region shifts to the wing's upper surface. In contrast, the low-pressure area appears on the lower surface, as observed in Fig. 17.

As the flapping motion progresses, the pressure mentioned above and vortex structures continue to be observed consecutively on the upper and lower surfaces of the wings.

3.3 Vortex Identification

To further analyze the flow patterns surrounding the wing, the patterns of vortices observed at different moments are depicted utilizing the non-dimensional Q-criterion (Hunt et al., 1988). The second invariant of velocity gradient (Q-criterion), also called the second invariant of the mean rate-of-displacement tensor, is given by Equation (5):

$$Q = \frac{1}{2}\left(\Omega_{ij}\Omega_{ij} - S_{ij}S_{ij}\right) = -\frac{1}{2}\frac{\partial u_i}{\partial x_j}\frac{\partial u_j}{\partial x_i} \tag{5}$$

In the Cartesian system, the velocity gradient is the summation of the symmetrical rate-of-strain (deformation) tensor S_{ij} and the skew-symmetrical rate-of-rotation tensor Ω_{ij}, which are given by:

$$S_{ij} = \frac{1}{2}\left(\frac{\partial u_i}{\partial x_j} + \frac{\partial u_j}{\partial x_i}\right) \tag{6}$$

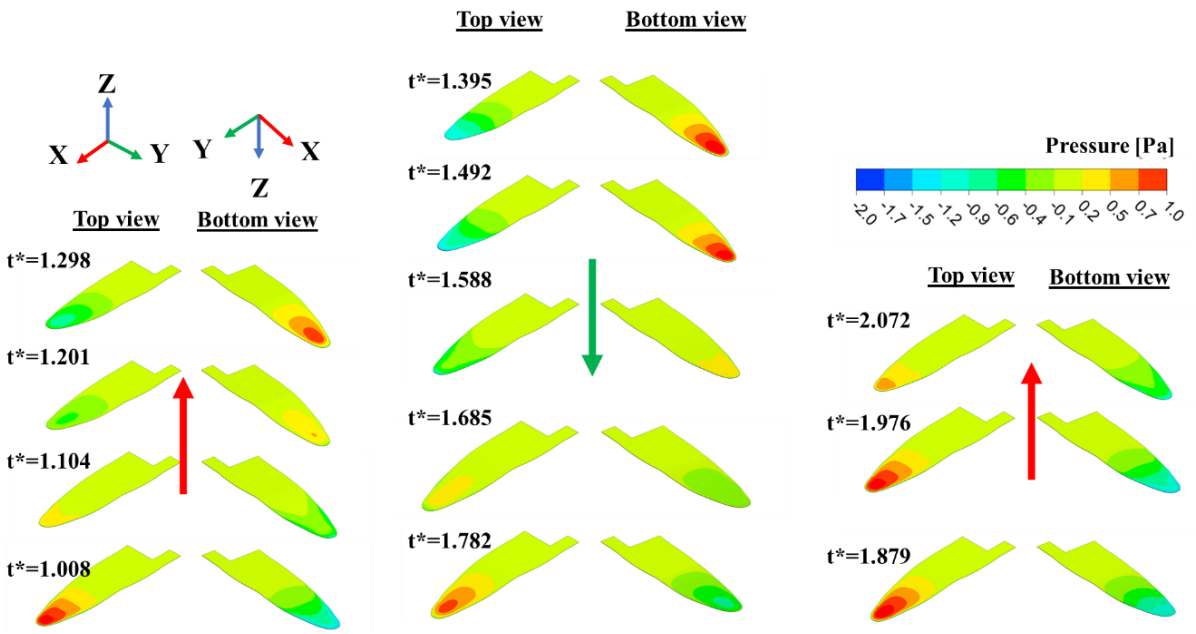

Fig. 17 Instantaneous pressure contours of rufous hummingbird wing (2nd period of flapping motion)

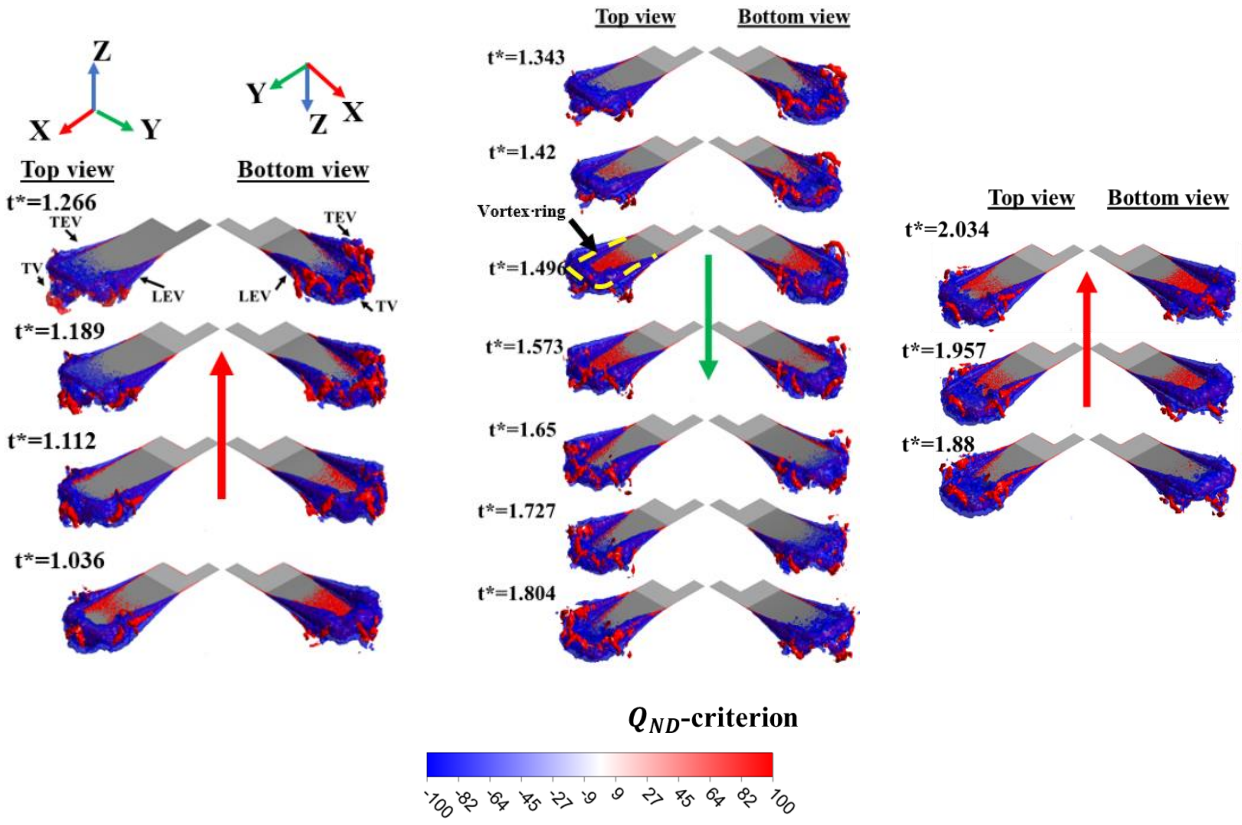

Fig. 18 Isosurface of non-dimensional Q criterion colored during one flapping cycle (rectangle wing, blue: negative, red: positive vortices)

$$\Omega_{ij} = \frac{1}{2}\left(\frac{\partial u_i}{\partial x_j} - \frac{\partial u_j}{\partial x_i}\right) \quad (7)$$

The non-dimensional Q_{ND} is defined as:

$$Q_{ND} = \frac{Q \cdot A}{(U_{tip})^2} \quad (8)$$

where A is the wing area, U_{tip} is the maximum velocity of the profile.

Through analysis of the Q-criterion of the wings, the three primary vortex structures - namely, the leading-edge vortex (LEV), the trailing-edge vortex (TEV), and the tip vortex (TV) - are observed in Fig. 18 and Fig. 19.

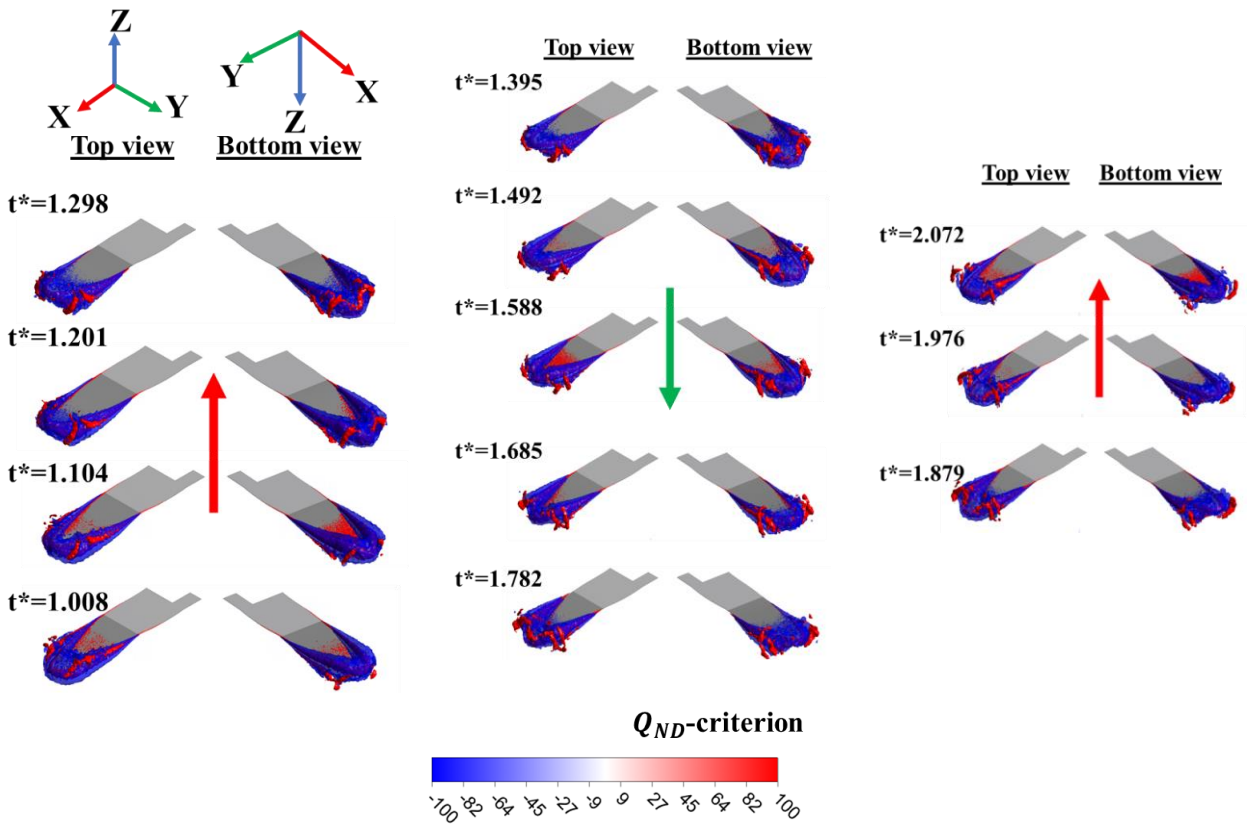

Fig. 19 Isosurface of non-dimensional Q criterion colored during one flapping cycle (hummingbird wing, blue: negative, red: positive vortices)

At t*=1.036, the rectangular wing begins its upstroke, while the hummingbird wing reaches this stage at t*=1.008. The vortices generated in the preceding stroke advance toward detachment from the wing, thereby priming for the genesis of new vortices. Furthermore. upon the wing returning to the stationary position, the leading-edge vortex (LEV) remains present on the upper surface. However, this LEV gradually migrates toward the wingtips and initiates detachment from the wing surface.

A ring vortex developed progressively from the previous period tends to break away as the wings move upward, transitioning from the upper side to the lower side of the wing. This conduct lasts from the end of the upstroke till the mid-downstroke. A new ring vortex appears on the upper surface of the wings at the start of the mid-downstroke. This formation is maintained during the upstroke and downstroke due to the wings' periodic flapping motion.

In particular, the leading-edge vortex (LEV) and trailing-edge vortex (TEV) are critical in establishing the orientation of the high-pressure area along the surfaces of a rectangular wing. At t*=1.266, the wing achieves its maximum positive flap angle, causing all vortex formations to remain underneath and increasing pressure levels along its lower surface. The peak pressure is notably near the wing's center at that time. After the wing's end of the downstroke, a reversal occurs in the direction of vortex movement. Notably, the tip vortices expand, with the vortex core manifesting at the tip of the upper wing surface at t*=1.496. Consequently, the high-pressure zone on the wing's lower surface migrates toward the wingtip. Upon reaching the maximum negative flap angle at t*=1.727, all vortex structures ascend to the upper wing surface, resulting in elevated pressure levels on the upper surface and an accompanying distribution of low pressure along the wing's lower surface (refer to Fig. 15 and Fig. 18).

Upon examining the displacement curve depicted in Fig. 14, it is evident that t*=1.266, the wing has reached its maximum upward position. At this moment, the force curve in Fig. 12 indicates the maximum force value. Additionally, at this position, the LEV-TEV and TV vortex structures in Fig. 18 are observed to spread from the wing's leading and trailing edges and the wingtip. These vortices remain below the wing and trail along with it. Consequently, at the onset of the downward motion, the wing is prepared for the arrival of new vortices and disperses existing ones from its surfaces.

At t*=1.496, the wing reaches a flat position as the force value approaches zero. This indicates a lack of sufficient inertial force at this point. However, Fig. 6 shows that aerodynamic forces have a tiny contribution at this instant. The impact of this force is discernible from the vortex structures observed in CFD analyses, wherein growing and accumulating vortices moving toward the wingtip are detected. Further analysis of relevant graphs reveals that when the wing reaches its lowest position, the force value indicates contributions from inertial and aerodynamic forces.

The wing structure of the Rufous hummingbird is examined in a way similar to that of a rectangular wing. Time instances, denoted as t*= 1.298, t*= 1.898, and t*=1.782, are illustrated in Fig. 16. A comparison with the rectangular wing demonstrates that the Rufous hummingbird generates relatively minor forces, as depicted in Fig. 7, Fig. 9, Fig. 11, and Fig. 13, respectively. This distinction can be ascribed to wing shape variances in various vortex configurations. As illustrated in Fig. 19, the vortex structures of the Rufous hummingbird exhibit a more constricted morphology, contrasting with the rectangular wing. Notably, these vortices exhibit minimal departure from the wing surfaces. The pressure distribution regions on both the upper and lower surfaces of the rectangular and hummingbird wing shapes show similar patterns throughout the entire motion despite the differences in their shapes.

5. CONCLUSION

Investigating force generation in bio-inspired flapping wings utilizes experimental and numerical techniques. The current study uses these methodologies to analyze the piezoelectrically actuated flapping wing mechanism. Thus, the generation of aerodynamic and inertial forces can be observed. The results of a comparative analysis between numerical findings (CFD+Inertial) and experimental outcomes (load cell) reveal a close agreement, particularly in the z-direction (vertical forces).

In the current study, digital image correlation (DIC) technology accurately captures dynamic deformations in the piezoelectric actuated flapping wings. These dynamic deformation data are then integrated into the computational fluid dynamics (CFD) solver to incorporate aeroelastic effects, eliminating the need for a complex fluid-structure interaction (FSI) model. By leveraging this data, the inertial forces exerted on the wing are computed, considering the flexibility effect, thereby providing a comprehensive understanding of the forces at play. In addition to force comparison, the study examines pressure distribution and vortex structures derived from CFD simulations. As mentioned in the previous section, at the beginning of the downstroke, a significant low-pressure area emerges on the wing's upper surface due to the tip vortex (TV) and the leading-edge vortex (LEV). At the same time, a consistent high-pressure region develops on the lower surface from remnants of vortices from the preceding stroke. Principal extremum values primarily result from pressure differentials across the upper and lower wing surfaces. The pressure distribution regions are interchanged after the mid-downstroke. At hover conditions, with zero-free stream velocity, vortical structures are solely carried by self-induction, leading to their proximity to the wing and the formation of a complex interference structure around it.

The differentiation of the wing models should be taken into account. Even when flapped by the same piezoelectric actuator under the same conditions, it is clear that rectangular and Rufous hummingbird wings have different flapping frequencies. This value is measured as 9.6 Hz for the rectangular wing model, while for the Rufous hummingbird, it is 12.1 Hz.

The maximum displacement observed is 11.6 mm for the rectangular wing and 9.4 mm for the Rufous hummingbird wing at their respective flapping frequencies. The displacement patterns of the two wings also vary. These measurements are used in computational fluid dynamics (CFD) models.

Total force values were obtained using load cell assistance alongside displacement measurements in the experimental setup. Thus, experimental data and numerical calculations obtained outputs related to displacement, force, pressure, and vortices for the rectangular wing and the Rufous hummingbird. In load cell measurements, a maximum force of 18.1 gr F_z was measured for the rectangular wing and 15.9 gr for the hummingbird wing. The results of the inertial force derived from displacement measurements and the F_z forces output by CFD calculations were 16.7 gr for the rectangular wing and 17.4 gr for the hummingbird wing.

From the force plots, it is observed that the graph consisting of inertial and CFD forces in the rectangular wing remains below the load cell data during the wing's upward motion. As a result, the rectangular wing mass, estimated at 7.8 grams, causes this behaviour. In contrast, it can be noted that the sum of inertial and CFD forces in the hummingbird wing (6.24 gr) surpasses the value recorded by the load cell. This observation suggests that the unique aerodynamic shape and the reduced weight of the hummingbird's wing contribute significantly to its efficiency of motion.

As a result of CFD analyses, the distributions seen in the pressure distribution contours are consistent with the upward and downward movements of the wings. However, the pressure distribution contours on the surface of the rectangular wing have wider transition intervals. In both wings, high and low-pressure regions concentrate at the wingtips. Additionally, when examining the vortex structures, it is observed that the LEV-TEV and TV structures on the rectangular wing are more chaotic and more significant at the wingtip. In contrast, the vortex structures on the hummingbird wing are smaller and less dispersed on the wing surfaces.

One significant constraint of our research is the inability to incorporate a pitching angle into the experimental setup for wing flapping driven by piezoelectricity using 1 DOF. Using a four-bar-like mechanism, piezoelectric actuators can be used to amplify the amplitudes and to superimpose pitch angles to the flapping motion.

ACKNOWLEDGEMENTS

This work is funded by the Scientific and Technological Research Council of Turkey under grant number TUBİTAK 116M273.

CONFLICT OF INTEREST

There are no conflicts to disclose.

AUTHORS CONTRIBUTION

Fadile Yudum Comez: Conceptualization, methodology, data collection, validation, formal analysis, writing, and editing of the original draft. **Nevsan Sengil:** Conceptualization, methodology, manuscript revision. **Dilek Funda Kurtulus:** Conceptualization, methodology, manuscript revision.

REFERENCES

ARAMIS v6.3. (2009, August 7). User Manual-Software. https://www.scribd.com/document/381257801/aramis-v6-1-pdf

Bektaş, M., Güler, M. A., & Kurtulus, D. F. (2020). One-way FSI analysis of bio-inspired flapping wings. *International Journal of Sustainable Aviation (IJSA)*, *6*(3). https://doi.10.1504/IJSA.2020.10034459

Comez, F. Y., Sengil, N., & Kurtulus, D. F. (2024). Three-dimensional flow evaluation of monarch butterfly wing. *Progress in Computational Fluid Dynamics, an International Journal*, *24*(4), 191-203. https://doi.org/10.1504/PCFD.2023.10058561

Dong, Y., Song, B., Xue, D., Li, Y., & Yang, W. (2022). Numerical study of the aerodynamics of a hovering hummingbird's wing with dynamic morphing. *International Journal of Aerospace Engineering*, *2022*(1), 5433184. https://doi.org/10.1155/2022/5433184.

Dwivedi, Y. D., Sudhir, S. Y. B., Sunil, B., Moorthy, C. H. V. K. N. S. N., & Allamraju, K. V. (2022). Numerical study of bio-inspired corrugated airfoil geometry in a forward flight at a low Reynolds number. *WSEAS Transactions on Fluid Mechanics*, *17*, 119-127. https://doi.org/10.37394/232013.2022.17.12

Fluent 6.3. (2006, September). UDF Manual. https://romeo.univ-reims.fr/documents/fluent/fluentUDFmanual.pdf

Hunt, J. C. R., Wray, A. A., & Moin, P. (1988). *Eddies, stream, and convergence zones in turbulent flows*. Report CTR-S88, Center for Turbulence Research.

James, J., Iyer, V., Chukewad, Y., Gollakota, S., & Fuller, S. B. (2018). *Liftoff of a 190 mg laser powered aerial vehicle: the lightest wireless robot to fly*. IEEE International Conference on Robotics and Automation (ICRA), IEEE. https://doi.10.1109/ICRA.2018.8460582.

Kurtulus, D. F. (2022). Critical angle and fundamental frequency of symmetric airfoils at low reynolds numbers. Journal of Applied Fluid Mechanics, 15(3), 723-735. https://doi.org/10.47176/jafm.15.03.33099

Kurtulus, D. F., Farcy, A., & Alemdaroglu, N. (2005, 10-13 Jan). *Unsteady aerodynamics of flapping airfoil in hovering flight at low reynolds numbers*. 43rd AIAA Aerospace Sciences Meeting and Exhibit, Reno, Nevada, USA.

Lau, E. M., Kumar, D., Chiang, C. H., Zhang, J. D., Huang, W. X., & Khare, V. (2020). *Pressure distribution of a deformable composite flapping wing*. Sensors and Smart Structures Technologies for Civil, Mechanical, and Aerospace Systems, 113790M. https://doi.org/10.1117/12.2558461

Ozaki, T., & Hamaguchi, K. (2018). Bioinspired flapping-wing robot with direct-driven piezoelectric actuation and its takeoff demonstration. *Robotics and Automation Letters*, *3*, 4217–4224. https://doi.10.1109/LRA.2018.2863104

Quinn Andrew, O. (2022). Efficacy of Flapping-wing Flight Via Dual Piezoelectric Actuation (Publication No. 11096) [M.Sc. Thesis, Rochester Institute of Technology]. Digital Institutional Repository. https://repository.rit.edu/theses/11096.

Senol, M. G., Arikan, K. B, & Kurtulus, D. F. (2017, 9-13 January). *Experimental and numerical results of a flapping wing four bar mechanism*. 55th AIAA Aerospace Sciences Meeting, Grapevine, Texas, AIAA 2017-0498. https://doi.org/10.2514/6.2017-0498.

Shyy, W., Aono, H., Kang, C., & Liu, H. (2013). *An introduction to flapping wing aerodynamics*. Cambridge University Press, ISBN 978-1-107-03726-7 Hardback.

Wu, P., & Ifju, P. (2010, 12-15 April). *Experimental methodology for flapping wing structure optimization in hovering flight of micro air vehicles*, AIAA 2010-2709, 51st AIAA/ASME/ASCE/AHS/ASC Structures, Structural Dynamics, and Materials Conference 18th, Orlando, Florida. https://doi.org/10.2514/6.2010-2709.

Yang, X., Song, B., Yang, W., Xue, D., Pei, Y., & Lang, X. (2022). Study of aerodynamic and inertial forces of a dovelike flapping-wing MAV by combining experimental and numerical methods. *Chinese Journal of Aeronautics*, *35*(6), 63–76. https://doi.org/10.1016/j.cja.2021.09.020

Zou, Y., Zhang, W., Ke, X., Lou, X., & Zhou, S. (2017). The design, and microfabrication of a sub 100 mg insect-scale flapping-wing robot. *Micro & Nano Letters.* *12*, 297–300. https://doi.org/10.1049/mnl.2016.0687